International Journal of Geo-Information

MDPI

Article

Spatial and Temporal Analysis of the Mitigating Effects of Industrial Relocation on the Surface Urban Heat Island over China

Linlin Zhang [1,2,3], Qingyan Meng [1,3,*], Zhenhui Sun [1,2,3] and Yunxiao Sun [1,2,3]

1 Institute of Remote Sensing and Digital Earth, Chinese Academy of Sciences, Beijing 100101, China; zhangll@radi.ac.cn (L.Z.); sunzh@radi.ac.cn (Z.S.); sunyx@radi.ac.cn (Y.S.)
2 University of Chinese Academy of Sciences, Beijing 100101, China
3 Sanya Institute of Remote Sensing, Sanya 572029, China
* Correspondence: mengqy@radi.ac.cn; Tel.: +86-010-6485-2195

Academic Editors: Bernd Resch and Wolfgang Kainz
Received: 28 February 2017; Accepted: 13 April 2017; Published: 19 April 2017

Abstract: Urbanization is typically accompanied by the relocation and reconstruction of industrial areas due to limited space and environmental requirements, particularly in the case of a capital city. Shougang Group, one of the largest steel mill operators in China, was relocated from Beijing to Hebei Province. To study the thermal environmental changes at the Shougang industrial site before and after relocation, four Landsat images (from 2000, 2005, 2010 and 2016) were used to calculate the land surface temperature (LST). Using the urban heat island ratio index (URI), we compared the LST values for the four images of the investigated area. Following the relocation of Shougang Group, the URI values decreased from 0.55 in 2005 to 0.21 in 2016, indicating that the surface urban heat island effect in the area was greatly mitigated; we infer that this effect was related to steel production. This study shows that the use of Landsat images to assess industrial thermal pollution is feasible. Accurate and rapid extraction of thermal pollution data by remote sensing offers great potential for the management of industrial pollution sources and distribution, and for technical support in urban planning departments.

Keywords: industrial relocation; remote sensing; thermal pollution; urban heat island; urban planning

1. Introduction

The world's urban population has grown rapidly, from approximately 0.7 billion in 1950 to almost 3.9 billion in 2014, and it is expected to reach 6.3 billion by 2050, a potential increase of more than two-thirds [1]. Rapid urbanization of human society results in increasing replacement of natural landscapes by impervious surfaces, which can alter surface radiation, thermal properties, and humidity over urban areas [2]. Anthropogenic waste heat generated through energy use by industry, traffic, and buildings has long been recognized as a contributor to the urban heat island (UHI) [3–7]. Recently, many industries located in urban areas have experienced excess capacity problems; such problems are especially common in the steel, coal, cement and power industries, which change land surface thermal radiance and contribute to industrial heat pollution and thermal anomalies [8–11]. Thus, accurate and rapid extraction of thermal pollution data has great potential in the management of industrial pollution sources and distribution.

China is a typical example of the inevitable trend of increasing urbanization [8]. Dramatic industrialization and rapid economic growth over recent decades have turned the country into a global factory, and one of the largest global energy consumers [12,13]. The distribution of

anthropogenic heat flux over China has been studied based on data from the Chinese Statistical Yearbook, and results imply that thermal pollution will become increasingly serious with the rapid growth of urbanization, resulting in substantial regional climate change and air pollution [14]. Consequently, it is especially important for Chinese cities to rapidly inventory sources of thermal pollution, and take steps toward its mitigation. For this reason, we have chosen the Shougang industrial site in China as our study area.

Thermal pollution can be evaluated by air temperature (AT) and satellite land surface temperature (LST) measurements [15]. AT and LST correspond to each other because the AT at the Earth's surface is controlled by the thermal properties of the underlying surface; however, the temperature dynamics and spatial variability in temperature values in atmospheric UHIs and surface urban heat islands (SUHIs) can differ greatly. AT is typically measured at approximately 5 feet (1.5 m) above the ground by weather stations, which use high temporal resolution [16–21]. However, due to the sparse distribution of observation stations, spatially continuous analysis is difficult. To solve this problem, the use of satellite data for the detection and assessment of SUHIs has been attempted [22–26]. Remote sensing data have wall-to-wall continuous coverage of urban areas [27]. Therefore, LST data derived from thermal infrared remote sensors have become commonly used indicators for heat island analysis [15].

Numerous studies have examined the relationship between SUHIs and urban planning. Significant mean temperature differences associated with different types of zoning in Indianapolis have been found using enhanced thematic mapper (ETM+) remote sensing data [28]. In a study of residential development patterns and UHI formation in Atlanta, lower-density residential development patterns were found to contribute more radiant heat energy to surface heat island formation than did higher-density development patterns [29]. Anthropogenic buildings were found to have pronounced UHI effects on a rapidly urbanizing arid region compared with an adjacent rural region [30]. Land usage has been shown to influence SUHIs; industrial, commercial, and residential areas, and airports and parks, exhibit high daytime temperatures [31]. Temperatures differ between industrial and commercial areas with grass and impervious surfaces [32].

Studies such as those cited above have focused on land cover and land use at the city scale; few have investigated the effects of functional area reconstruction on SUHIs. The objective of this study was to analyze the influence of industrial relocation on the thermal environment using Landsat data for the case of the Shougang Group in Beijing, China. To compare LST values from remote sensing data for different periods, we used the urban heat island ratio index (URI). We then performed spatial and temporal analysis of the SUHI to detect changes in thermal pollution due to the relocation process. Finally, the relationships between the SUHI and land cover type, URI, and steel production were examined to determine the cause of the mitigation of thermal pollution following the relocation of the Shougang industrial site.

2. Materials and Methods

2.1. Study Area

The Shougang industrial site was located at 116°7′43″ E–116°11′51″ E and 39°53′14″ N–39°55′43″ N in the Shijingshan District of Beijing City, 18 km from Tiananmen Square. It was bordered to the west by the Yongding River (Figure 1). The area of the study site is 9.98 km^2. Shougang Group is one of the largest operators of steel mills in China, engaging in high-emission production processes including coking, sintering, ironmaking, steelmaking, and steel rolling (Figure 1d). Industrial processes release large amounts of waste heat, causing the loss of usable energy and environmental pollution. With approval from the State Council, the Shougang Group relocated from Beijing beginning in 2005, ending production at the investigated site in 2010. Shougang was then reconstructed as a new industrial park.

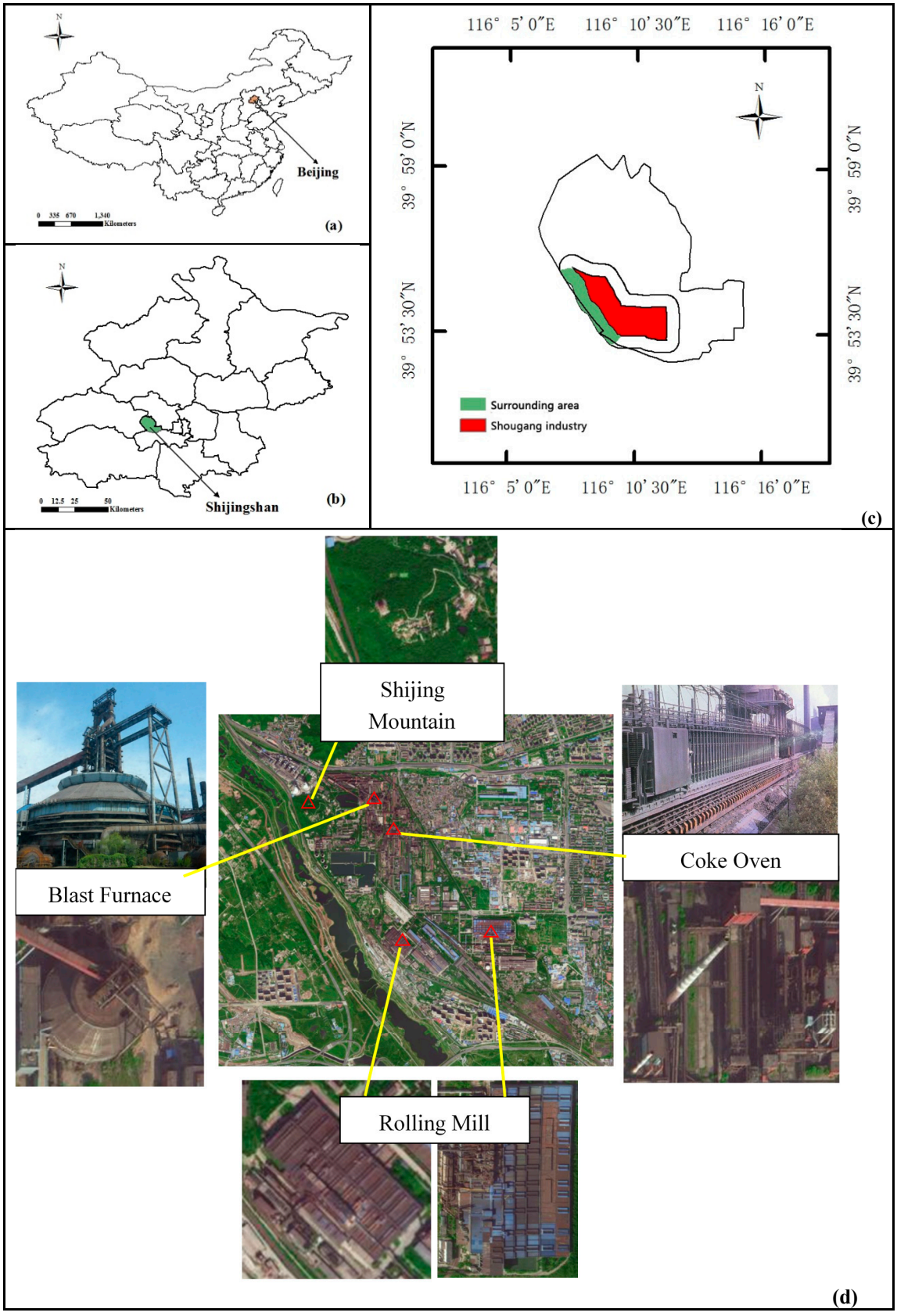

Figure 1. Location of the study area. (**a**) Beijing, China. (**b**) The administrative boundary of Shijingshan District, Beijing. (**c**) The Shougang industrial area (red) and Surrounding area (green) in Shijingshan District. (**d**) Shougang Group production equipment used before relocation.

2.2. Data Acquisition

Landsat images used in this study were downloaded from the United States Geological Survey data archive. Images from October 30, 2000; May 4, 2005; and May 20, 2010 were collected by the Landsat 5 Thematic Mapper (TM), and that from April 18, 2016 was collected by the Landsat 8 Operational Land Imager (OLI). The spatial resolution of the TM and OLI images was 30 m.

2.3. Work Flow

The overall work flow was composed of four steps (Figure 2): LST retrieval, URI calculation, SUHI analysis, and determination of the relationships between thermal pollution and land cover types and steel production. Four Landsat images were used in the first step to calculate LST. These results were generated using the radiance transfer equation, which includes apparent radiance, land surface emissivity (LSE), and radiance of blackbody calculations. In the second step, we used a normalization method and a density-slicing classification technique to complete LST-level distribution. We then calculated the URI, to compare LST data from different periods. Based on these results, we conducted spatial and temporal SUHI analysis for the Shougang industrial site and the surrounding area. Finally, we analyzed the relationship between the SUHI and land cover types, and that between the URI and steel production.

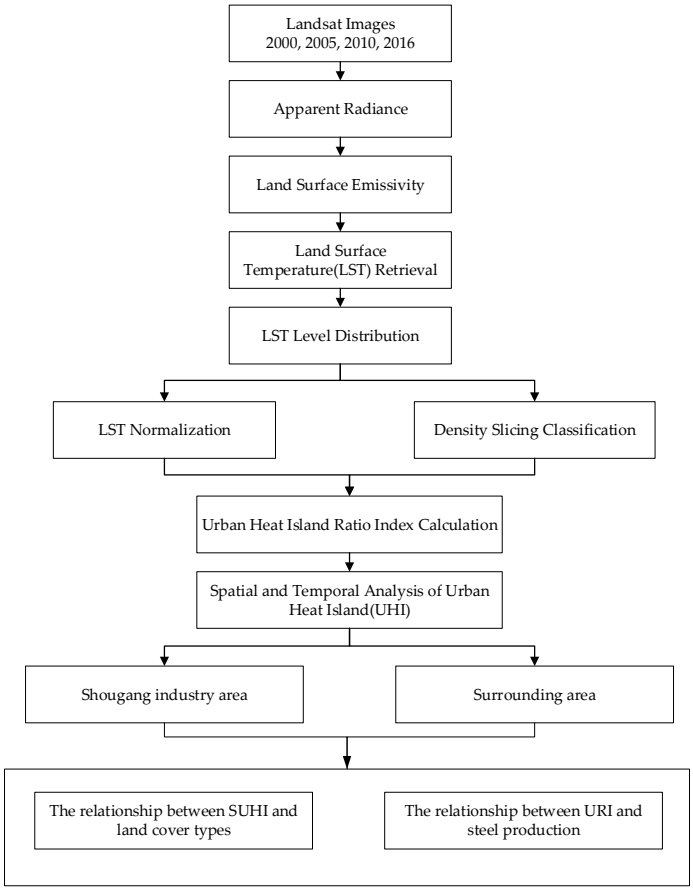

Figure 2. Flow chart for the study.

2.4. LST Retrieval

Landsat TM data comprise one thermal band (band 6), whereas Landsat 8 data have two (bands 10 and 11). Because band 11 has a running fault, we used a radiance transfer equation (single channel) to retrieve LST:

$$L_{sensor} = [\varepsilon B(T_s) + (1-\varepsilon)L^{\downarrow}_{atm}]\tau + L^{\uparrow}_{atm} \quad (1)$$

where T_s is the LST(k); L_{sensor} is the apparent radiance ($W{\cdot}m^{-2}{\cdot}sr^{-1}{\cdot}\mu m^{-1}$), acquired by image calibration; $B(T_s)$ is the blackbody radiance under temperature T_s, based on Planck's law ($W{\cdot}m^{-2}{\cdot}sr^{-1}{\cdot}\mu m^{-1}$); $L^{\uparrow}_{\text{atm}}$ and $L^{\downarrow}_{\text{atm}}$ are the upwelling and downwelling atmospheric radiances, respectively ($W{\cdot}m^{-2}{\cdot}sr^{-1}{\cdot}\mu m^{-1}$); τ is the atmospheric transmittance, retrieved from the National Aeronautics and Space Administration (NASA) website (http://atmcorr.gsfc.nasa.gov/); ε is the ground emissivity, calculated using the near-infrared and visible bands.

2.4.1. Apparent Radiance

Apparent radiance is calculated by converting the digital number (DN) value to pupil radiance. For Landsat data, the equation is:

$$L_{sensor} = Gain * DN + Offset \quad (2)$$

where *Gain* and *Offset* are the Landsat thermal infrared band values. For the TM data, *Gain* = 0.0553 and *Offset* = 1.1824; for the Landsat 8 data, *Gain* = 0.0003 and *Offset* = 0.1000.

2.4.2. Land Surface Emissivity

LSE is required when LST is retrieved based on the radiance transfer equation. The normalized difference vegetation index (NDVI) is typically used to acquire LSE [33–36]. In this study, we used the following LSE calculation method. Based on mixed-pixel decomposition, objects were classified as water, vegetation or buildings. The value of water emissivity was 0.995; natural surface and building emissivities were calculated by the following equations, respectively [36]:

$$\varepsilon_{\text{soil}} = P_v R_v \varepsilon_v + (1-P_v) R_s \varepsilon_s + d\varepsilon \quad (3)$$

$$\varepsilon_{building} = P_v R_v \varepsilon_v + (1-P_v) R_m \varepsilon_m + d\varepsilon \quad (4)$$

R_v, R_s, and R_m are the temperature ratios of pure vegetation, soil, and building pixels, respectively: R_v = 0.9332 + 0.0585P_v, R_s = 0.9902 + 0.1068P_v, and R_m = 0.9886 + 0.1287. ε_v, ε_s, ε_m are the emissivities of pure vegetation, soil, and building pixels, respectively, where ε_v = 0.986, ε_s= 0.972, ε_m = 0.970. dε is the terrain geometry; when the terrain is flat, dε = 0. P_v is the vegetation coverage, calculated by the following equation:

$$P_v = \left[\frac{NDVI - NDVI_{\text{min}}}{NDVI_{\text{max}} - NDVI_{\text{min}}}\right]^2 \quad (5)$$

where $NDVI_{max}$ = 0.70, $NDVI_{min}$ = 0.05 [37,38], When a pixel's NDVI value is > 0.7, P_v = 1; when a pixel's *NDVI* value is < 0.05, P_v = 0.

2.4.3. Land Surface Temperature Retrieval

We obtained the downwelling and upwelling atmospheric radiances $L^{\downarrow}_{\text{atm}}$ and $L^{\uparrow}_{\text{atm}}$ and the atmospheric transmittance τ from the NASA website (http://atmcorr.gsfc.nasa.gov/), by entering parameters including time, longitude and latitude of the investigated area, atmospheric model, and sensor type. Radiance of the blackbody *B (Ts)* can be calculated based on Equation (1). Land surface temperature, T_s, can then be calculated based on the Planck inverse function,

$$T_s = K_2 / \ln(K_1 / B(T_s) + 1) \quad (6)$$

K_1 and K_2 are calibration constants, which differ according to the scan type. For TM data, K_1 = 607.76 W/(m^2·sr·μm) and K_2 = 1260.56 K; for Landsat 8 data, K_1 = 774.89 W/(m^2·sr·μm) and K_2 = 1321.08 K.

2.5. LST Level Distribution

Direct comparison of thermal data for different periods using absolute LST values is inappropriate [39]. Thus, a normalization method was used to compare the calculated LST data from the four study years. The LST images were rescaled to the same level between 0 and 1 using the maximum and minimum values for those images. The equation is as follows:

$$T_{\mathrm{i}} = \frac{T_{si} - T_{\mathrm{smin}}}{T_{\mathrm{smax}} - T_{\mathrm{smin}}} \quad (7)$$

where T_i is the normalized value of i_{th} pixel, T_{si} is the LST of the i_{th} pixel, T_{smax} is the maximum value of that image, and T_{smin} is the minimum value of that image.

The normalized LST images were divided into five temperature levels using the density-slicing classification technique [40], with the lowest value assigned to level 1 and the highest to level 5. The area change of each temperature level before and after relocation of the Shougang industrial area was analyzed (Table 1, Figure 3a–d).

Table 1. Temperature levels, 2000–2016.

Levels	2000		2005		2010		2016		2005–2016
	Area		Area		Area		Area		Area
	Km^2	%	Km^2	%	Km^2	%	Km^2	%	Km^2
1	0.13	1.26	0.26	2.57	0.79	7.89	0.13	1.30	−0.13
2	1.10	10.97	0.64	6.37	1.06	10.61	1.07	10.73	0.43
3	4.88	48.92	2.74	27.49	3.96	39.63	6.18	61.90	3.44
4	2.42	24.26	4.33	43.41	2.78	27.89	2.52	25.21	−1.81
5	1.45	14.59	2.01	20.16	1.39	13.98	0.08	0.86	−1.93
Total	9.98	100	9.98	100	9.98	100	9.98	100	

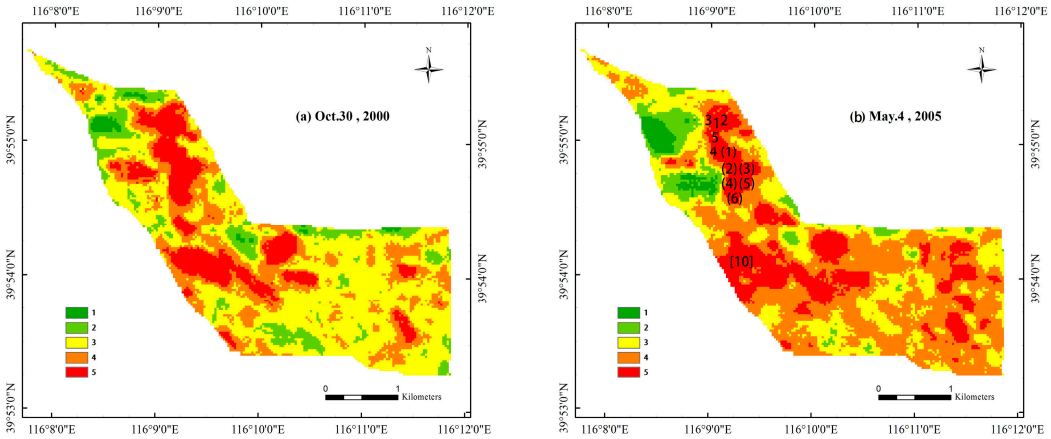

Figure 3. *Cont.*

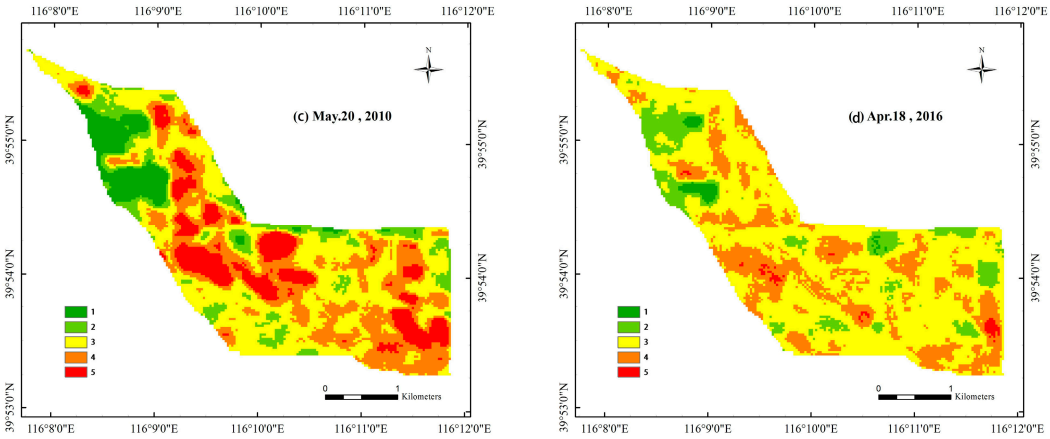

Figure 3. LST levels distribution of Shougang industrial area in different periods. (**a**) 30 October 2000; (**b**) 4 May 2005; (**c**) 20 May 2010; (**d**) 18 April 2016. Equipment distribution: 1–5 represent No. 1 BF to No. 5 BF, respectively; (1)–(6) represent No. 1 CO to No. 6 CO, respectively; [10] represent RM. Where BF represents Blast Furnace, CO represents Coke Oven, RM represents Rolling Mill.

2.6. Uban Heat Island Ratio Index

To assess the difference in SUHI effect among the four years, we used the URI, which was proposed to compare SUHI differences between periods quantitatively [41]. A larger URI value indicates a more serious SUHI effect. The URI is expressed as follows:

$$URI = \frac{1}{100m}\sum_{i=1}^{n} W_i P_i \tag{8}$$

where m is the number of divided temperature levels and n is the number of temperature levels that are higher than those in surrounding areas. W_i is a weight value determined using the value of the corresponding level (i), and p_i is the percentage of the area of level i with respect to the entire area.

In this study, temperature values were higher in the areas of levels 4 and 5 than in the surrounding area. In such a case, m is 5; n is 2; w_1 and w_2 are 4 and 5, respectively; and p_i can be obtained from Table 1. Accordingly, the URIs for 2000, 2005, 2010 and 2016 were calculated as follows:

$$URI_{(2000)} = \frac{1}{100*5}(5*14.59+4*24.26) = 0.34$$
$$URI_{(2005)} = \frac{1}{100*5}(5*20.16+4*43.41) = 0.55$$
$$URI_{(2010)} = \frac{1}{100*5}(5*13.98+4*27.89) = 0.36$$
$$URI_{(2016)} = \frac{1}{100*5}(5*0.86+4*25.21) = 0.21$$

2.7. Building Area Extraction

To evaluate changes due to land cover type, an index-based built-up index (IBI) was used to extract building areas. This thematic-oriented technique was proposed to delineate building area from nonbuilding area, based on three existing indices: the soil-adjusted vegetation index (SAVI), the modified normalized difference water index (MNDWI), and the normalized difference built-up index (NDBI) [42]. The IBI clearly separates the spectral clusters of three major urban components: built-up land, vegetation and water. It is expressed as follows:

$$IBI = \frac{NDBI - \frac{SAVI + MNDWI}{2}}{NDBI + \frac{SAVI + MNDWI}{2}} \quad (9)$$

In this study, we used the *IBI* to detect changes in building and nonbuilding areas in the Shougang industrial area during the study period (Figure 4).

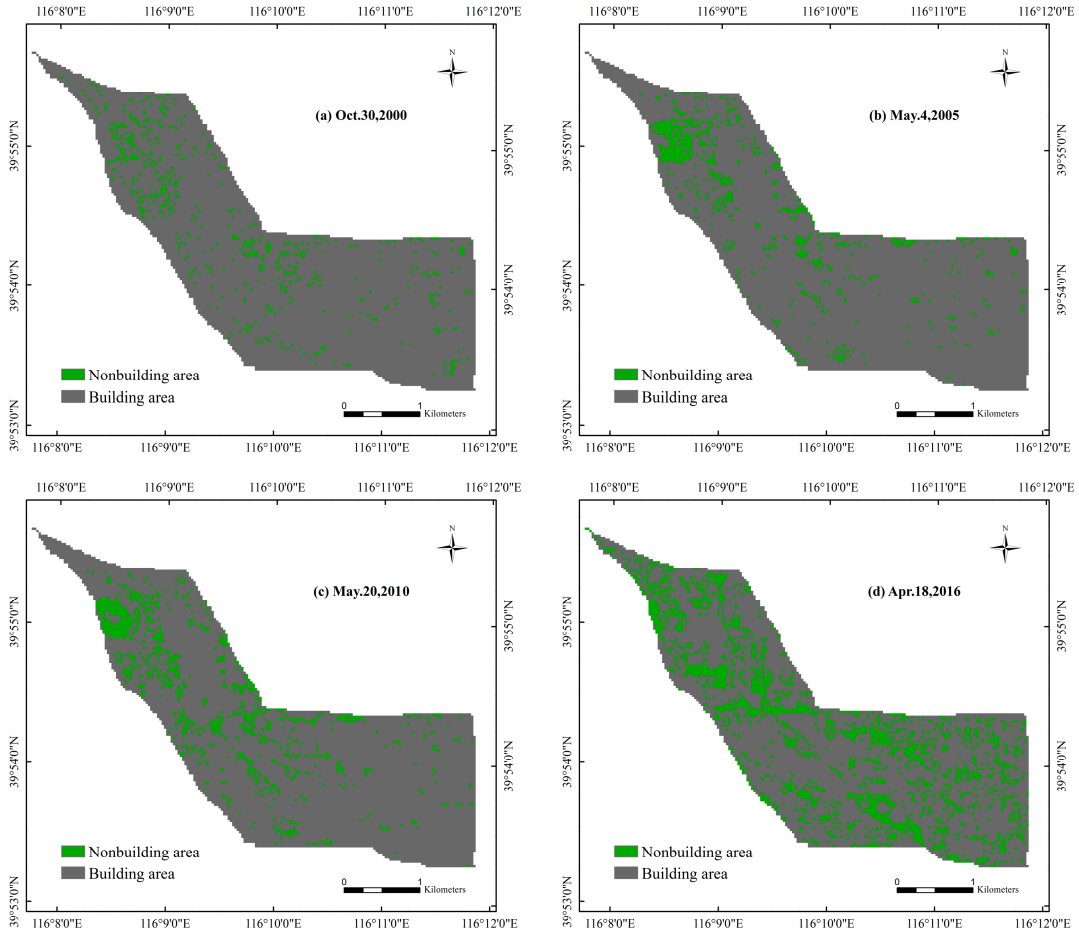

Figure 4. Distribution of building and nonbuilding areas at the Shougang industrial site during different periods. (**a**) 30 October 2000; (**b**) 4 May 2005; (**c**) 20 May 2010; and (**d**) 18 April 2016.

3. Results and Discussion

3.1. SUHI Change Analysis

3.1.1. Temporal Analysis of SUHI Changes in the Shougang Industrial Area

Urban construction in China was in a stage of rapid development between 2000 and 2005, concurrent with yearly increases in steel production at the Shougang industrial site. During this period, the area represented by temperature levels 4 and 5 increased from 38.85% to 63.57% (Figure 3a,b), and the URI value increased from 0.34 to 0.55. Beginning in 2005, the Shougang Group relocated gradually to a coastal area in Hebei Province. Steel production decreased annually in the investigated area, and production was halted until the end of 2010. Although steel production continued in May 2010, the SUHI effect was apparently lower than in 2005 (Figure 3c); the area represented by temperature levels 4 and 5 decreased by 21.7%, and the URI value decreased from 0.55 to 0.36. Since its relocation, the Shougang Group has focused on building the New Shougang High-end Comprehensive

Service Area in the investigated area, making it a "green," low-carbon demonstration garden. Many of the industrial ruins have been preserved; former factories have been divided into an industrial theme park, culture creative industry, comprehensive serving center, headquarters economy zone, and business development complex. By 2016, level 5 temperatures had almost disappeared (Figure 3d) and the URI had decreased to 0.21. Overall, the SUHI was greatly mitigated in the investigated area.

To study the dynamics of the SUHI in the investigated area following the Shougang relocation and reconstruction, the image difference technique was applied based on density slicing of LST images from 2005 and 2016. The produced difference image (Figure 5) shows the patterns of change in the SUHI between 2005 and 2016. A general decrease of the SUHI over these 11 years is illustrated, as the green patches representing decreased temperature areas are larger and more numerous than the red patches representing increased temperature areas. Quantitatively, the area representing high temperature levels (4 and 5) decreased by 63.57% to 26.07% between 2005 and 2016. The calculated URI also suggests that the Shougang area SUHI was substantially mitigated. Many high-temperature areas, such as those where the blast furnace (BF) and rolling mill (RM) were located, disappeared.

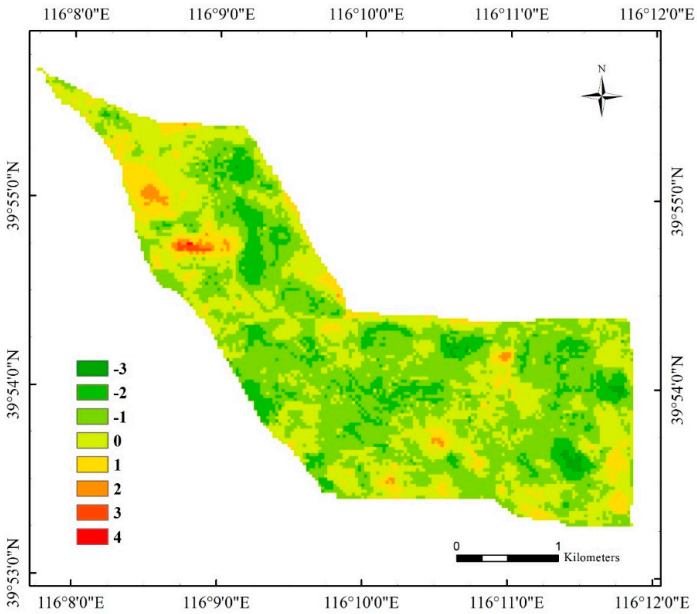

Figure 5. Changes in temperature levels between 2005 and 2016 in Shougang.

3.1.2. Spatial Analysis of SUHI Changes in the Shougang Industrial Area

The Shougang Group expanded its steel production from 803 million tons in 2000 to 1044.12 million tons in 2005. During this period, the area representing temperature levels 4 and 5 expanded by 2.47 km^2. The proportion of red patches reached a maximum during the four years examined in this study. Since the commencement of relocation, the Shougang Group has gradually reduced production. For example, the No. 5 BF stopped production in 2005, the No. 1 BF and No. 2 coke oven (CO) stopped in 2006, the No. 4 BF and two converters at the No. 3 steel mill stopped in 2007, and the entire No. 3 steel mill stopped in 2008, until the end of production at the No. 3 BF signaled the completion of the Shougang relocation project. As of 20 May 2010, the Shougang Group had not yet stopped production; the No. 3 BF and part of the steel mill remained in operation. Accordingly, these operating areas were high-temperature areas, where the SUHI phenomenon persisted (Figure 3c). However, in areas where production had stopped, such as the BF and CO areas, LST levels were significantly lower. Following relocation and reconstruction, the area representing temperature level 5 decreased significantly, to 0.86%. The difference image shows green patches over formerly high-temperature areas, such as those where the BF, CO, and RM were located, with temperature reductions of up to 3 °C.

3.1.3. Thermal Changes in the Surrounding Area

The minimum area influenced by a SUHI effect has been determined to be 150% of an urban area in SUHI-related research [43]. To study the effects of the Shougang Group on the surrounding area before and after relocation, part of 150% of the Shougang industrial area was selected as the surrounding area (Figure 1c, green area).

Images of the distribution of LST levels in 2005 and 2016 and a difference image were acquired using the same data processing method used to create the Shougang industrial area image (Figure 6). Green patches (level 1) near the Yongding River increased substantially following the Shougang industrial area relocation. Red patches (levels 4 and 5), which represent residential areas, also increased, possibly due to man-made, engineered infrastructure.

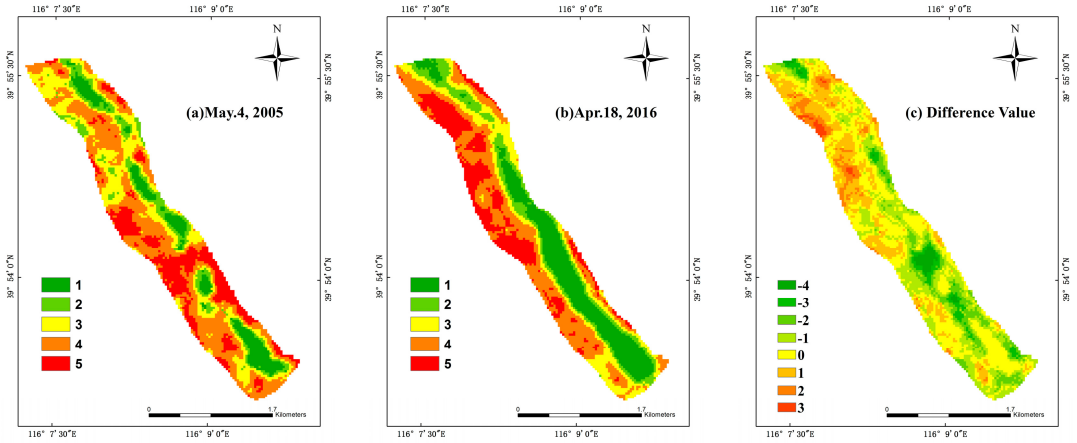

Figure 6. Temperature level distribution of the area surrounding the Shougang industrial site. (**a**) 4 May 2005; (**b**) 18 April 2016; (**c**) difference between (**a**) and (**b**).

3.2. The Relationship between SUHI and Land Cover Type

UHI intensity is related to patterns of land use and land cover change (LUCC); e.g., the composition of vegetation, water, and building land, and changes therein [44].To determine the reason for SUHI intensity changes in the Shougang industrial area, we used the IBI to extract the building and nonbuilding areas in the four years studied (Figure 4). We calculated the percentages of pixels representing building and nonbuilding areas (Table 2).

Table 2. Pixels representing building and nonbuilding areas, 2000–2016.

Land Cover Type	2000		2005		2010		2016	
	Pixels	Percent	Pixels	Percent	Pixels	Percent	Pixels	Percent
Nonbuilding	835	7.53%	610	5.50%	1162	10.48%	2526	22.77%
Building	10,258	92.47%	10,483	94.50%	9931	89.52%	8567	77.23%

Corresponding to industrial relocation, the percentage of building area decreased from 94.50% to 77.23%, and the URI decreased from 0.55 to 0.21. The number of pixels for each LST level differed between building and nonbuilding areas. We inferred that land cover type might be related to LST; accordingly, we developed statistics describing the effects of LST level distribution on LUCC (Figures 4 and 5). We calculated the frequency of LST levels 1–5 in building and nonbuilding areas, and created histograms and normal distribution curves (Figure 7). The gray histogram represents the distribution frequency of each LST level in building areas, and green represents nonbuilding areas. Means (μ) and standard deviations (σ) are presented in Figure 7.

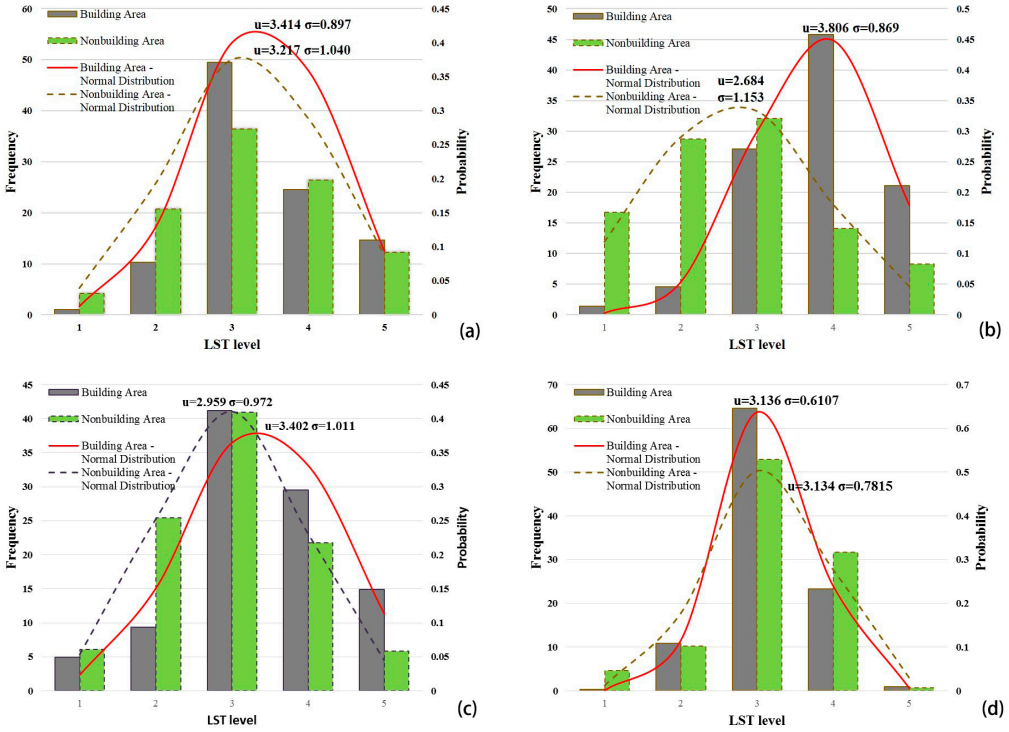

Figure 7. The frequency of LST levels 1–5 in building and nonbuilding areas. (**a**) 30 October 2000; (**b**) 4 May 2005; (**c**) 20 May 2010; (**d**) 18 April 2016.

In the building areas, the mean LST level increased (from 3.414 to 3.806) during periods of industrial development (2000–2005) and decreased (from 3.806 to 3.136) during the relocation period (2005–2016). The standard deviation represents the degree of dispersion of the LST level distribution. A smaller σ value indicates that the data distribution was more aggregated. During the development and relocation periods, 2005 and 2016, σ was smaller in the Shougang industrial area, indicating that LST levels were more aggregated. In 2005, the most frequent LST level was 4, due to the release of abundant thermal pollution during steel production. In 2016, the most frequent LST level was 3, due to the relocation of the Shougang industrial area, which caused decreases in artificial heat and building areas. The mean value of each LST level in the nonbuilding areas was lower than that in the building areas. Most of the production equipment in the Shougang industrial area was preserved, such that the building areas decreased by only 17.27% following the relocation, with very little LUCC. We conclude that the mitigation of UHI intensity was due mainly to the halting of steel production. Some studies have indicated that differences in UHI can be attributed to three factors: the production of anthropogenic energy, the effects of energy transformation in cities, and a decrease in evapotranspiration [24].

3.3. The Relationship between URI and Steel Production

Steel production data for each study year were collected from the Shougang Group website (http://www.shougang.com.cn/). Regression analysis was performed to determine the relationship between the URI and steel production using several regression models, including linear, exponential, polynomial, logarithmic, and power models. The results show that the URI was correlated positively with steel production, indicating that the increase in steel production contributed to thermal pollution in the region (Figure 8). Among regression models, the exponential model produced the highest R^2 value, demonstrating an exponential relationship between the URI and steel production.

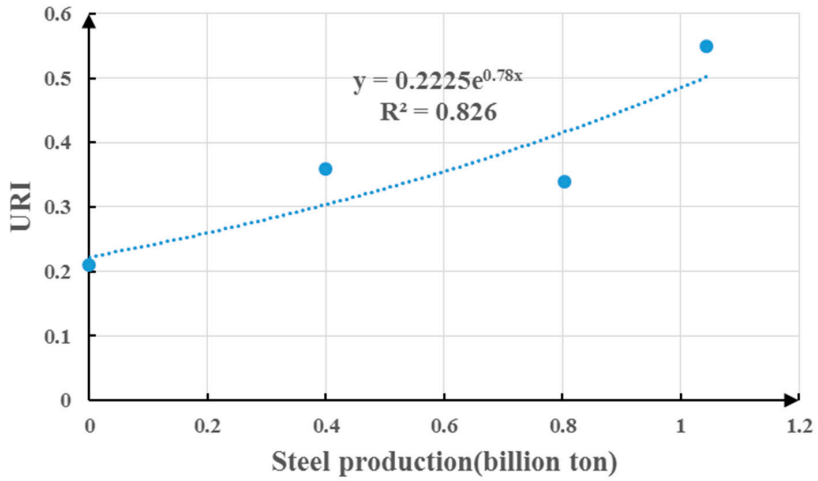

Figure 8. Regression analysis of the relationship between urban heat island ratio index (URI) and steel production.

4. Conclusions

Remote sensing technology, characterized by airborne and satellite-based Earth observation platforms, provides an effective way to continuously monitor changing processes on the landscape [45]. We used four Landsat images to detect thermal changes due to industrial relocation. The remote sensing technique enabled convenient and efficient detection of thermal pollution. The normalization method, density-slicing technique, and URI were used to compare temperatures recorded in different periods. Spatial and temporal SUHI analysis indicated that the relocation and reconstruction of the Shougang industrial area significantly mitigated thermal pollution, in the thermal source area and the surrounding area. The URI of the Shougang industrial area decreased from 0.55 in 2005 to 0.21 in 2016. The relocation process removed thermal sources, such as BFs and an RM. The surrounding area, including the Yongding River, experienced significant thermal mitigation following the relocation of the industrial area. The IBI was used to detect changes in building and nonbuilding areas. By analyzing the mean LST level for different land cover types, we found that SUHI mitigation in the Shougang industrial area was due mainly to the halting of steel production, as land cover types changed very little. We examined the relationship between URI and steel production, and found that the increase in steel production contributed to a rise in thermal pollution in the region. This study showed that Landsat thermal infrared data can be used to detect thermal pollution and monitor changes in capacity. Thermal pollution has become a serious problem in China due to rapid urbanization. Thus, this study will be of great significance in detecting thermal anomalies and providing technical support for urban planning departments.

Although this work has contributed to progress in the application of remote sensing technologies to detect thermal pollution, and determined the relationship between thermal pollution and steel production, other factors, such as the iron and steel smelting processes, may influence energy release. Therefore, more research needs to be conducted to discover the influence of production technology on the thermal environment.

Acknowledgments: This work was supported by Hainan Province Natural Science Foundation Innovative Research Team: Study on Urban Green Landscape Pattern Remote Sensing Evaluation based on Lidar and Multispectral Data [2017CXTD015], Guangdong Province Science and Technology Project: Urban Impervious Surface Remote Sensing Extraction System [2016A050502065], Sichuan Province Science and Technology Support Program: Chengdu City Impervious Surface Remote Sensing Extraction System [2016JZ0027] and Hainan Province Natural Science Foundation: Urban Heat Island Remote Sensing Retrieval Technology in Urban Main Construction Area based on Night Light Index [417219].

Author Contributions: Linlin Zhang designed and implemented the data analysis methods and wrote the manuscript. Qingyan Meng supervised the data analysis, edited the manuscript. Zhenhui Sun and Yunxiao Sun assisted with the data analysis and manuscript preparation.

Conflicts of Interest: The authors declare no conflict of interest.

References

1. United Nations. *World Urbanization Prospects: The 2014 Revision*; Department of Economic and Social Affairs, Population Division, United Nations: New York, NY, USA, 2014.
2. Wang, K.; Wang, J.; Wang, P.; Sparrow, M.; Yang, J.; Chen, H. Influences of urbanization on surface characteristics as derived from the moderate-resolution imaging spectroradiometer: A case study for the Beijing metropolitan area. *J. Geophys. Res. Atmos.* **2007**. [CrossRef]
3. Flanner, M.G. Integrating anthropogenic heat flux with global climate models. *Geophys. Res. Lett.* **2009**. [CrossRef]
4. Ichinose, T.; Shimodozono, K.; Hanaki, K. Impact of anthropogenic heat on urban climate in Tokyo. *Atmos. Environ.* **1999**, *33*, 3897–3909. [CrossRef]
5. Kato, S.; Yamaguchi, Y. Analysis of urban heat-island effect using aster and ETM+ data: Separation of anthropogenic heat discharge and natural heat radiation from sensible heat flux. *Remote Sens. Environ.* **2005**, *99*, 44–54. [CrossRef]
6. Khan, S.M.; Simpson, R.W. Effect of a heat island on the meteorology of a complex urban airshed. *Boundary-Layer Meteorol.* **2001**, *100*, 487–506. [CrossRef]
7. Simmonds, I.; Keay, K. Weekly cycle of meteorological variations in Melbourne and the role of pollution and anthropogenic heat release. *Atmos. Environ.* **1997**, *31*, 1589–1603. [CrossRef]
8. Zhao, X.; Jiang, H.; Wang, H.; Zhao, J.; Qiu, Q.; Tapper, N.; Hua, L. Remotely sensed thermal pollution and its relationship with energy consumption and industry in a rapidly urbanizing Chinese city. *Energy Policy* **2013**, *57*, 398–406. [CrossRef]
9. Nordell, B. Thermal pollution causes global warming. *Global Planet. Change* **2003**, *38*, 305–312. [CrossRef]
10. Lu, D.; Weng, Q. Spectral mixture analysis of ASTER images for examining the relationship between urban thermal features and biophysical descriptors in Indianapolis, Indiana, USA. *Remote Sens. Environ.* **2006**, *104*, 157–167. [CrossRef]
11. Chen, Y.; Sui, D.; Fung, T.; Dou, W. Fractal analysis of the structure and dynamics of a satellite-detected urban heat island. *Int. J. Remote Sens.* **2007**, *28*, 2359–2366.
12. Wang, R.; Liu, W.; Xiao, L.; Liu, J.; Kao, W. Path towards achieving of China's 2020 carbon emission reduction target—A discussion of low-carbon energy policies at province level. *Energy Policy* **2011**, *39*, 2740–2747. [CrossRef]
13. Ye, H.; Wang, K.; Zhao, X.; Chen, F.; Li, X.; Pan, L. Relationship between construction characteristics and carbon emissions from urban household operational energy usage. *Energy Build.* **2011**, *43*, 147–152. [CrossRef]
14. Xie, M.; Zhu, K.; Wang, T.; Feng, W.; Zhu, X.; Chen, F.; Ouyang, Y.; Liu, Z. Study on the distribution of anthropogenic heat flux over China. *China Environ. Sci.* **2015**, *35*, 728–734.
15. Shen, H.; Huang, L.; Zhang, L.; Wu, P.; Zeng, C. Long-term and fine-scale satellite monitoring of the urban heat island effect by the fusion of multi-temporal and multi-sensor remote sensed data: A 26-year case study of the city of Wuhan in China. *Remote Sens. Environ.* **2016**, *172*, 109–125. [CrossRef]
16. Feyisa, G.L.; Dons, K.; Meilby, H. Efficiency of parks in mitigating urban heat island effect: An example from Addis Ababa. *Landsc. Urban Plan.* **2014**, *123*, 87–95. [CrossRef]
17. Parker, D.E. Urban heat island effects on estimates of observed climate change. *Wiley Interdiscip. Rev. Clim. Change* **2010**, *1*, 123–133. [CrossRef]
18. Velazquez-Lozada, A.; Gonzalez, J.E.; Winter, A. Urban heat island effect analysis for San Juan, Puerto Rico. *Atmos. Environ.* **2006**, *40*, 1731–1741. [CrossRef]
19. Oke, T.R. The energetic basis of the urban heat island. *Q. J. R. Meteorol. Soc.* **1982**, *108*, 1–24. [CrossRef]
20. Arnfield, A.J. Two decades of urban climate research: A review of turbulence, exchanges of energy and water, and the urban heat island. *Int. J. Climatol.* **2003**, *23*, 1–26. [CrossRef]
21. Li, X.; Zhou, W.; Ouyang, Z. Relationship between land surface temperature and spatial pattern of greenspace: What are the effects of spatial resolution? *Landsc. Urban Plan.* **2013**, *114*, 1–8. [CrossRef]
22. Yusuf, Y.A.; Pradhan, B.; Idrees, M.O. Spatio-temporal assessment of urban heat island effects in Kuala Lumpur metropolitan city using landsat images. *J. Indian Soc. Remote Sens.* **2014**, *42*, 829–837. [CrossRef]

23. Stathopoulou, M.; Cartalis, C. Downscaling AVHRR land surface temperatures for improved surface urban heat island intensity estimation. *Remote Sens. Environ.* **2009**, *113*, 2592–2605. [CrossRef]
24. Ogashawara, I.; da Silva Brum Bastos, V. A quantitative approach for analyzing the relationship between urban heat islands and land cover. *Remote Sens.* **2012**, *4*, 3596–3618. [CrossRef]
25. Melaas, E.K.; Wang, J.A.; Miller, D.L.; Friedl, M.A. Interactions between urban vegetation and surface urban heat islands: A case study in the boston metropolitan region. *Environ. Res. Lett.* **2016**, *11*, 054020. [CrossRef]
26. Imhoff, M.L.; Zhang, P.; Wolfe, R.E.; Bounoua, L. Remote sensing of the urban heat island effect across biomes in the continental USA. *Remote Sens. Environ.* **2010**, *114*, 504–513. [CrossRef]
27. Li, J.; Song, C.; Cao, L.; Zhu, F.; Meng, X.; Wu, J. Impacts of landscape structure on surface urban heat islands: A case study of Shanghai, China. *Remote Sens. Environ.* **2011**, *115*, 3249–3263. [CrossRef]
28. Wilson, J.S.; Clay, M.; Martin, E.; Stuckey, D.; Vedder-Risch, K. Evaluating environmental influences of zoning in urban ecosystems with remote sensing. *Remote Sens. Environ.* **2003**, *86*, 303–321. [CrossRef]
29. Stone, B., Jr.; Rodgers, M.O. Urban form and thermal efficiency: How the design of cities influences the urban heat island effect. *J. Am. Plan. Assoc.* **2001**, *67*, 186–198. [CrossRef]
30. Golden, J.S. The built environment induced urban heat island effect in rapidly urbanizing arid regions—A sustainable urban engineering complexity. *Environ. Sci.* **2004**, *1*, 321–349. [CrossRef]
31. Jusuf, S.K.; Wong, N.H.; Hagen, E.; Anggoro, R.; Hong, Y. The influence of land use on the urban heat island in Singapore. *Habitat Int.* **2007**, *31*, 232–242. [CrossRef]
32. Connors, J.P.; Galletti, C.S.; Chow, W.T. Landscape configuration and urban heat island effects: Assessing the relationship between landscape characteristics and land surface temperature in Phoenix, Arizona. *Landsc. Ecol.* **2013**, *28*, 271–283. [CrossRef]
33. Van de Griend, A.; Owe, M. On the relationship between thermal emissivity and the normalized difference vegetation index for natural surfaces. *Int. J. Remote Sens.* **1993**, *14*, 1119–1131. [CrossRef]
34. Valor, E.; Caselles, V. Mapping land surface emissivity from NDVI: Application to European, African, and South American areas. *Remote Sens. Environ.* **1996**, *57*, 167–184. [CrossRef]
35. Sobrino, J.; Raissouni, N.; Li, Z.-L. A comparative study of land surface emissivity retrieval from NOAA data. *Remote Sens. Environ.* **2001**, *75*, 256–266. [CrossRef]
36. Qin, Z.; Li, W.; Xu, B.; Chen, Z.; Liu, J. The estimation of land surface emissivity for landsat TM6. *Remote Sens. Land Resour.* **2004**, *3*, 28–32.
37. Ding, F.; Hu, H. Comparison of two new algorithms for retrieving land surface temperature from landsat TM thermal band. *Geo-Inf. Sci.* **2006**, *8*, 125–130.
38. Li, J.; Zhang, Q.; Zhu, Y.; Liu, L.; Ye, J. Land surface temperature retrieval and dynamic change of the thermal landsacpe patterns of Hefei city. *J. Anhui Agric. Univ.* **2012**, *39*, 629–636.
39. Tang, F.; Xu, H. The influence of urban reconstruction in urban heat island effect: Cangxia area of Fuzhou City, China. In Proceedings of the Seventeenth China Symposium on Remote Sensing, Hangzhou, China, 27–31 August 2010; Volume 8203, pp. 525–528.
40. Manavalan, P.; Sathyanath, P.; Rajegowda, G. Digital image analysis techniques to estimate waterspread for capacity evaluations of reservoirs. *Photogramm. Eng. Remote Sens.* **1993**, *59*, 1389–1395.
41. Xu, H.; Chen, B. A study on urban heat island and its spatial relationship with urban expansion: Xiamen, SE China. *Urban Stud.* **2004**, *2*, 013.
42. Xu, H. Extraction of urban built-up land features from landsat imagery using a thematicoriented index combination technique. *Photogramm. Eng. Remote Sens.* **2007**, *73*, 1381–1391. [CrossRef]
43. Peng, S.; Piao, S.; Ciais, P.; Friedlingstein, P.; Ottle, C.; Bréon, F.-M.; Nan, H.; Zhou, L.; Myneni, R.B. Surface urban heat island across 419 global big cities. *Environ. Sci. Technol.* **2011**, *46*, 696–703. [CrossRef] [PubMed]
44. Chen, X.-L.; Zhao, H.-M.; Li, P.-X.; Yin, Z.-Y. Remote sensing image-based analysis of the relationship between urban heat island and land use/cover changes. *Remote Sens. Environ.* **2006**, *104*, 133–146. [CrossRef]
45. Li, J.; Zhang, Y.; Wang, X.; Qin, Q.; Wei, Z.; Li, J. Application of GPS trajectory data for investigating the interaction between human activity and landscape pattern: A case study of the Lijiang River Basin, China. *ISPRS Int. J. Geo-Inf.* **2016**, *5*, 104. [CrossRef]